Orbitally forced ice sheet fluctuations during the Marinoan Snowball Earth glaciation

Benn, Douglas I.; Le Hir, Guillaume; Bao, Huiming; Donnadieu, Yannick; Dumas, Christophe; Fleming, Edward J.; Hambrey, Michael J.; Mcmillan, Emily A.; Petronis, Michael S.; Ramstein, Gilles; Stevenson, Carl T. E.; Wynn, Peter M.; Fairchild, Ian J.

Published in:
Nature Geoscience

DOI:
10.1038/ngeo2502

Publication date:
2015

Citation for published version (APA):
Benn, D. I., Le Hir, G., Bao, H., Donnadieu, Y., Dumas, C., Fleming, E. J., Hambrey, M. J., Mcmillan, E. A., Petronis, M. S., Ramstein, G., Stevenson, C. T. E., Wynn, P. M., & Fairchild, I. J. (2015). Orbitally forced ice sheet fluctuations during the Marinoan Snowball Earth glaciation. *Nature Geoscience*, *8*(9), 704-707. https://doi.org/10.1038/ngeo2502

Orbitally Forced Ice Sheet Fluctuations in Snowball Earth

Supporting Online Information

Douglas I. Benn, Guillaume Le Hir, Huiming Bao, Yannick Donnadieu, Christophe Dumas, Edward J. Fleming, Michael J. Hambrey, Emily A. McMillan, Michael S. Petronis, Gilles Ramstein, Carl T.E. Stevenson, Peter M. Wynn and Ian J. Fairchild

*Corresponding author. E-mail: Doug.Benn@unis.no

1. Additional descriptions of sediment facies

Detailed stratigraphic logs of all sections are shown in Figure S1, and the main divisions of the Wilsonbreen Formation as they appear in the field are shown in Figure S2. Seven lithofacies associations have been identified (Fig. S3).

FA1: *Subglacial*. This association consists of a) sheared diamictites with striated and faceted clasts of both intra-basinal and extra-basinal lithologies. b) boulder pavements (Fig. S4f); c) sheared, unconsolidated sediment derived from underlying strata (Fig. S4e); and d) channelized and deformed interbeds of sandstone and conglomerate (Fig. S4g). These are interpreted, respectively, as subglacial traction tills, horizons of lodged clasts marking former positions of the glacier bed; glacitectonite, and infills of subglacial channels. Clast shape is indicative of active transport below sliding ice (cf. Benn and Ballantyne, 1983), and clast and AMS fabrics are highly clustered, indicating shearing to high cumulative strains (cf. Benn, 1994). Shear direction is consistently towards the north and north-west (relative to the current orientation of Svalbard, but not taking account of any possible rotation of the land surface since the Neoproterozoic). Clasts of far-travelled extrabasinal clast lithologies (e.g. granite and gneiss) are common. The suite of sediment facies and structures is diagnostic of active, sliding ice over-riding unconsolidated sediment (Benn and Evans, 2010).

FA2: *Fluvial channels*. This association consists of interbeds of a) thin pebble conglomerates, b) cross-stratified sandstones, and c) stromatolitic limestone with very low relief growth domes (Fig. S5a, b, d). Basal erosion surfaces and internal surfaces

demonstrate lateral accretion of the sand bodies, indicating bar and channel migration under steady, unidirectional flows. The stromatolites display distinct millimetre-scale lamination with sandy laminae, interpreted as reflective of an annual regime of river flow. In addition, there are common occurrences of derived trains of intraclasts, reflecting erosion and reworking of stromatolites by fluvial action.

FA3: *Dolomitic floodplain*. Facies in this association include a) discrete zones of pronounced dolomite cementation within a sandstone or siltstone, with dolomite-cemented nodules and vuggy cavities, and b) dolomitic microbial laminites, with broad cm-scale stromatolitic domes. The displacive cementation is characteristic of calcretes in which mineral precipitation occurs as a response to evaporative losses at or above a water table (Fig. S5c). The microbial laminite deposits are distinct from laminar calcretes, but represent accretion on intermittently flooded subaerial surfaces colonized by microbial mats.

FA4: *Carbonate lake margin*. This association consists of rhythmic alternations of carbonate and sorted terrigenous sediment, in association with wave ripple lamination or desiccation structures (Fig. S5e, f). At Ditlovtoppen and Dracoisen there are, additionally, occurrences of a distinctive sandstone facies. This consists of highly uniform, well-sorted fine- to medium-grained sandstone, with very well-rounded grains. Bedding structures are confined to indistinct, discontinuous parallel stratification. The association is interpreted as sediment sorted and reworked by wave action, indicating an unfrozen water body. The well-rounded sand grains found in the sandstone beds are consistent with aeolian transport prior to deposition in water.

FA5: *Carbonate lacustrine*. This association is dominated by rhythmic alternations of finely crystalline or stromatolitic carbonates and poorly sorted clastic sediment (Fig. S5g, h). Microbial influence is widespread, in the form of irregular microbial lamination or stromatolitic domes. Clastic layers with pebble-sized fragments occur. These sediments were laid down in a water body lacking significant current activity. The clastic sediment is invariably very poorly sorted, contains diamictite pellets likely to be derived by ice rafting (till pellets) and local ice-rafted clasts (dropstones). Disturbance of partly lithified beds by downslope slumping is common.

FA6: *Glacilacustrine*. This association includes ice-proximal (FA6-G) and ice-distal (FA6-D) variants. The ice-proximal facies consists of sandstone and conglomerate clinoforms interbedded with diamictite, forming tapering wedge-shaped structures apparently thinning to the north and dipping 10° more steeply than the regional bedding (Fig. S4h, i). Convolute bedding and slump structures in the sandstones and conglomerates indicate local syn-depositional deformation. These are interpreted as grounding-line fans, deposited from episodic pulses of sorted sediment into a water body (Powell and Alley, 1997). The ice-distal facies consists predominantly of massive to weakly bedded diamictite, containing striated and faceted clasts of both intra- and extra-basinal lithologies. Wispy bedding and interbeds of laminated siltstone with occasional dropstones are present in places (Fig. S4d). In W2 and W3, carbonate lacustrine sediments occur as interbeds within the diamictite, and some of the carbonate horizons contain dropstones. The diamictites are interpreted as the product of rain-out of ice-rafted sediment and suspended fine sediment from meltwater plumes. Clast fabrics are typically girdles, consistent with a dropstone origin (Domack and Lawson, 1985).

Interbeds of sandstone and conglomerate occur within the diamictites, forming channelized lenses or more laterally extensive planar beds, recording intermittent mass flows.

In previous studies (e.g. Fairchild and Hambrey, 1995) some ice-rafted facies in members W1 and W3 were presumed to be glacimarine by default, but no specific justification for a marine rather than a lacustrine origin was presented. The close association of the diamictites with carbonate lacustrine sediments, some of which contain dropstones, and the occurrence of lacustrine and terrestrial facies throughout the succession, make a glacilacustrine origin much more likely. A glacimarine origin would require repeated incursions of the sea in phase with increased fluxes of glacigenic sediment, whereas a glacilacustrine interpretation simply requires episodic glacigenic sediment input to a closed, lacustrine basin. Furthermore, basal conglomerates indicative of marine transgression are absent, except at the base of the cap carbonate.

FA7: *Periglacial*. At the base of W1, this association consists of the brecciated upper surface of the dolostone of the preglacial Elbobreen Formation, and associated sandstones and isolated pebbles. The upper few decimeters of the dolostone are traversed by dense networks of sand-filled fractures, with fracture density increasing upward such that the upper levels consist of dolostone fragments floating in a matrix of sand (Fig. S4a). At the upper surface, thin layers of sand occur, within which are isolated facetted pebbles (Fig. 4b). Some of the pebbles have 'dreikanter' morphology and are interpreted as ventifacts (Knight, 2008). The association is interpreted as frost shattered rock with infilling of blown sand, overlain by thin layers of blown sand with wind-transported and sculpted pebbles. A second occurrence of the periglacial association is found at the base of W2. In contrast with the base of W1, this is developed in soft sediment (diamictites of the glacilacustrine and subglacial associations), and consists of sand-filled wedges and pebble lag horizons, interpreted as frost wedges and winnowed land surfaces.

The sedimentological evidence clearly shows that the depositional basin remained isolated from the sea from the time of formation of the periglacial weathering horizon until the basal Ediacaran transgression. The weathering horizon is developed in supra-tidal carbonates, indicating that the area was at sea level prior to deposition of the Wilsonbreen Formation. The isolation of the basin from the sea may appear inconsistent with the long timescale we propose for the Wilsonbreen Formation ($\sim 10^7$ years), due to the amount of crustal subsidence that can be expected over this period (perhaps 100-200 m at typical intracratonic subsidence rates of 0.01 mm yr^{-1}). For the late Marinoan period of high pCO_2, our modeled continental ice volumes are $\sim 1.5 \times 10^8$ km^3, equivalent to a mean eustatic sea-level fall of ~420 m. Detailed modeling by Creveling and Mitrovica (ref 14) indicated full-glacial Marinoan sea-levels of approx. -500 m in the Svalbard region. Isostatic depression from ice loading may be expected to cause additional subsidence during the glaciation. However, both the geological evidence and our modeling results indicate that the study area occupied a peripheral location with regard to the ice sheets, with only limited and relatively brief presence of glacier ice. Isostatic depression would therefore have been minor, and it is reasonable to conclude that eustatic sea-level fall more than offset both tectonic and isostatic subsidence in our study area until the onset of final deglaciation, allowing the basin to

remain isolated from the sea. Interestingly, net subsidence of ~200 m is consistent with the geological evidence, since the Wilsonbreen Formation was truncated to 180 m in thickness by the Ediacaran transgression.

Figure S1. Sedimentary logs of the Wilsonbreen Formation at the locations shown in Figure 1 of the main paper.
(N.B. This figure is large-format and is saved as a separate pdf file)

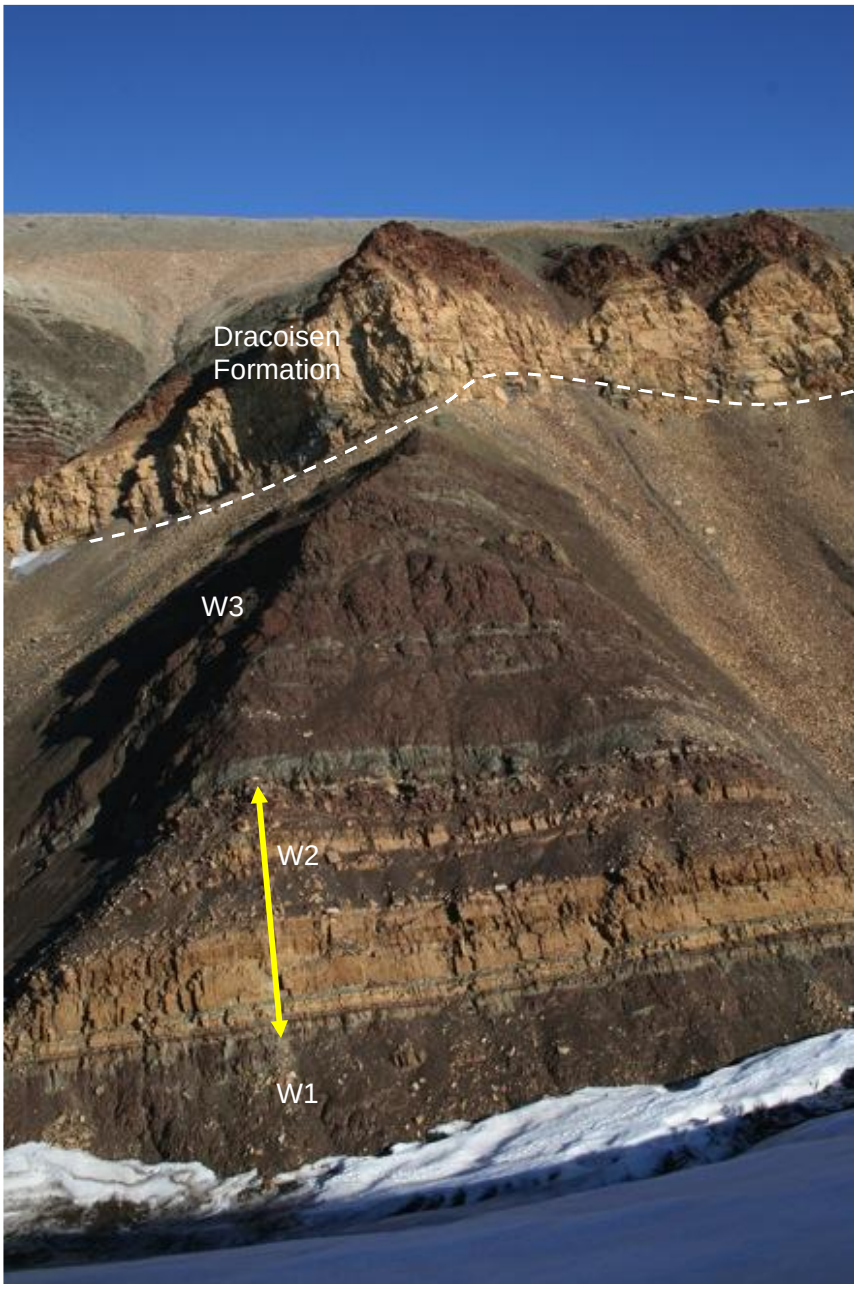

Figure S2. Upper members of the Wilsonbreen Formation and overlying Ediacaran (cap) carbonate of the Dracoisen Formation at Ditlovtoppen.

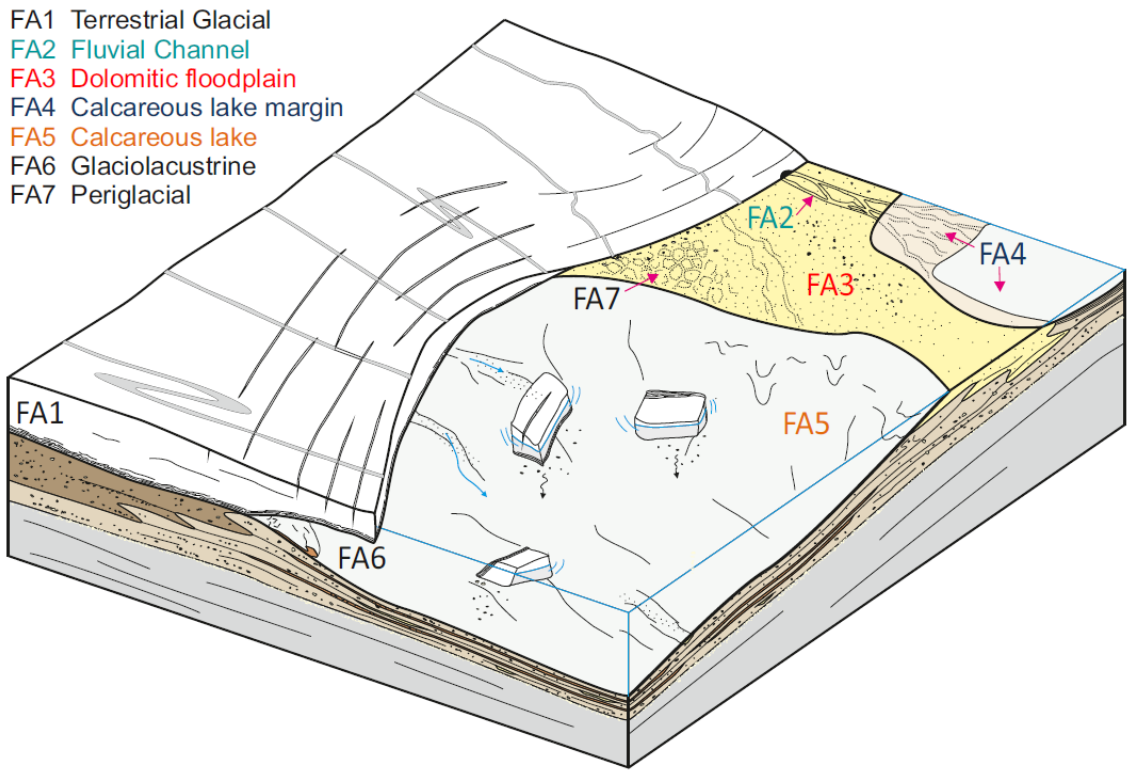

Figure S3: Facies Associations recognized in Members W2 and W3 of the Wilsonbreen Formation.


a


b

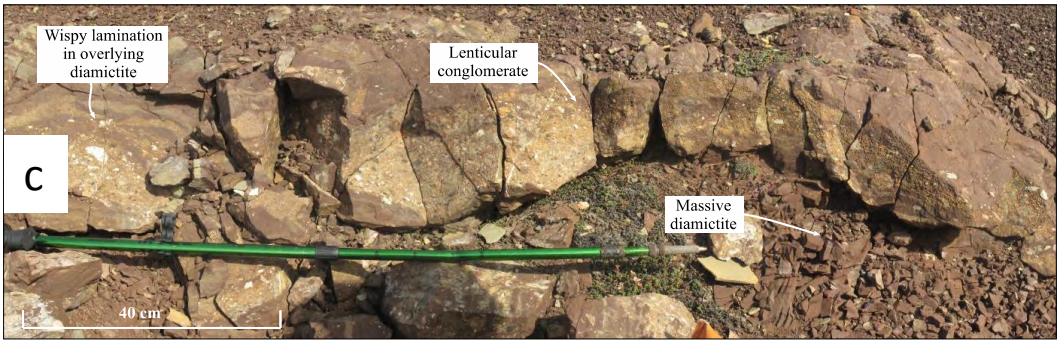
Wispy lamination in overlying diamictite
Lenticular conglomerate
Massive diamictite
40 cm
c


d

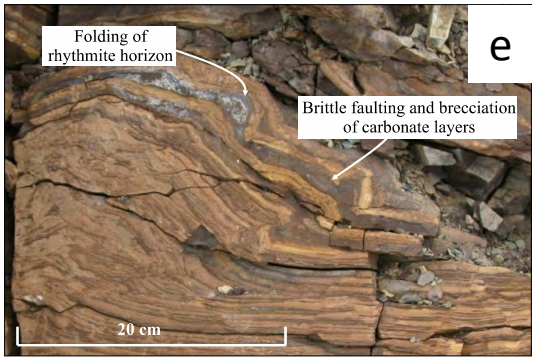
Folding of rhythmite horizon
Brittle faulting and brecciation of carbonate layers
20 cm
e


f


Sheared diamictite
Boulder with planed-off surface
Sandy channel fill
g

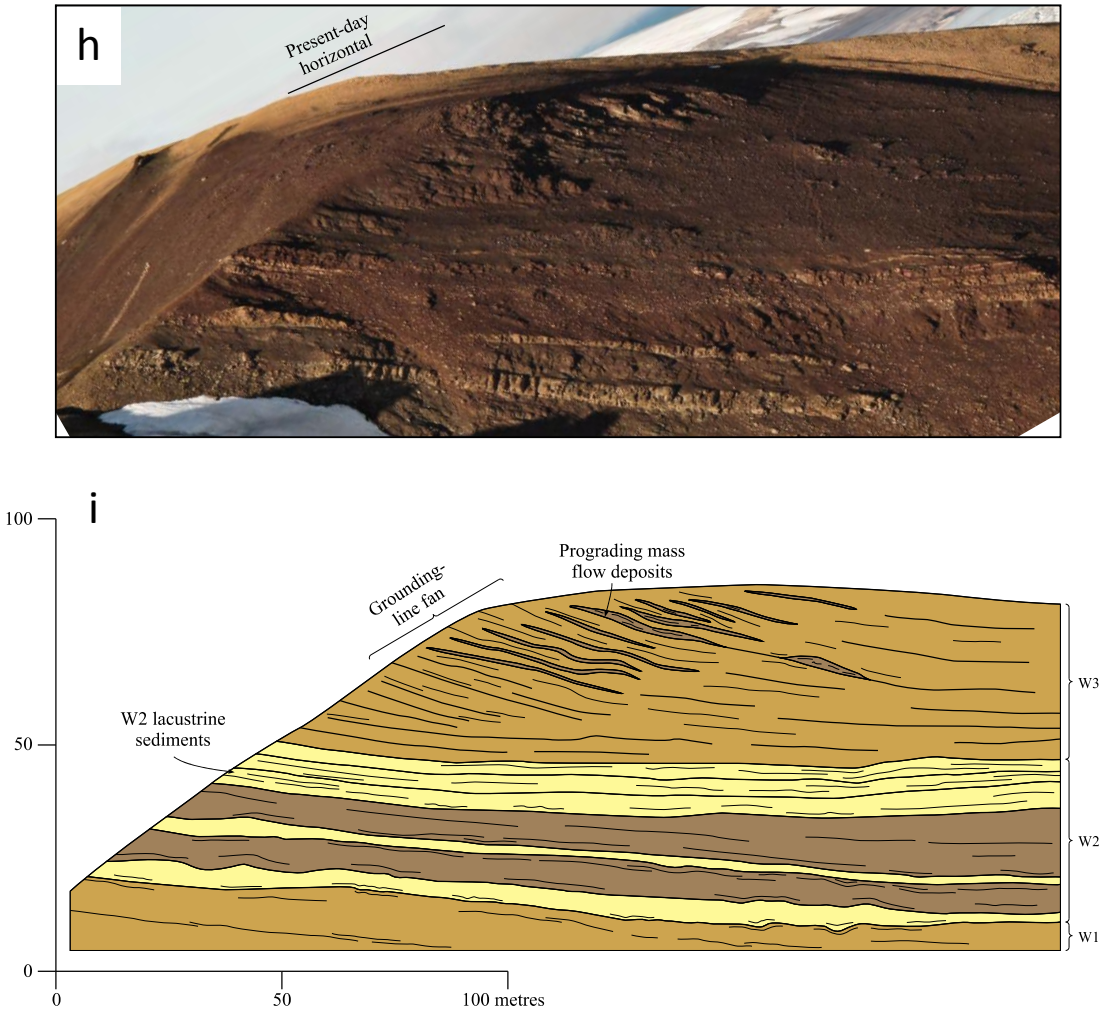

Figure S4. Periglacial and glacigenic sediments. (a) Frost shattered dolostone with sand infillings, base of member W1, Slangen. (b) Faceted pebble (ventifact), lower left, in dolostone (white) breccia with sand (brown) infillings, base of member W1, Dracoisen. (c) Conglomerate interbed (debris-flow) in diamictite, member W3, Dracoisen, from same stratigraphic level as mass flow deposits shown in (i). (d) Glacilacustrine diamictite with dropstones, member W1, McDonaldryggen. (e) Glacitectonized rhythmites, top of member W2, Ditlovtoppen. (f) Boulder pavement, member W3, Ditlovtoppen. (g) Faceted boulder lodged in subglacial channel fill, member W3, Ditlovtoppen. (h) and (i) Grounding line fan, member W3, Dracoisen.

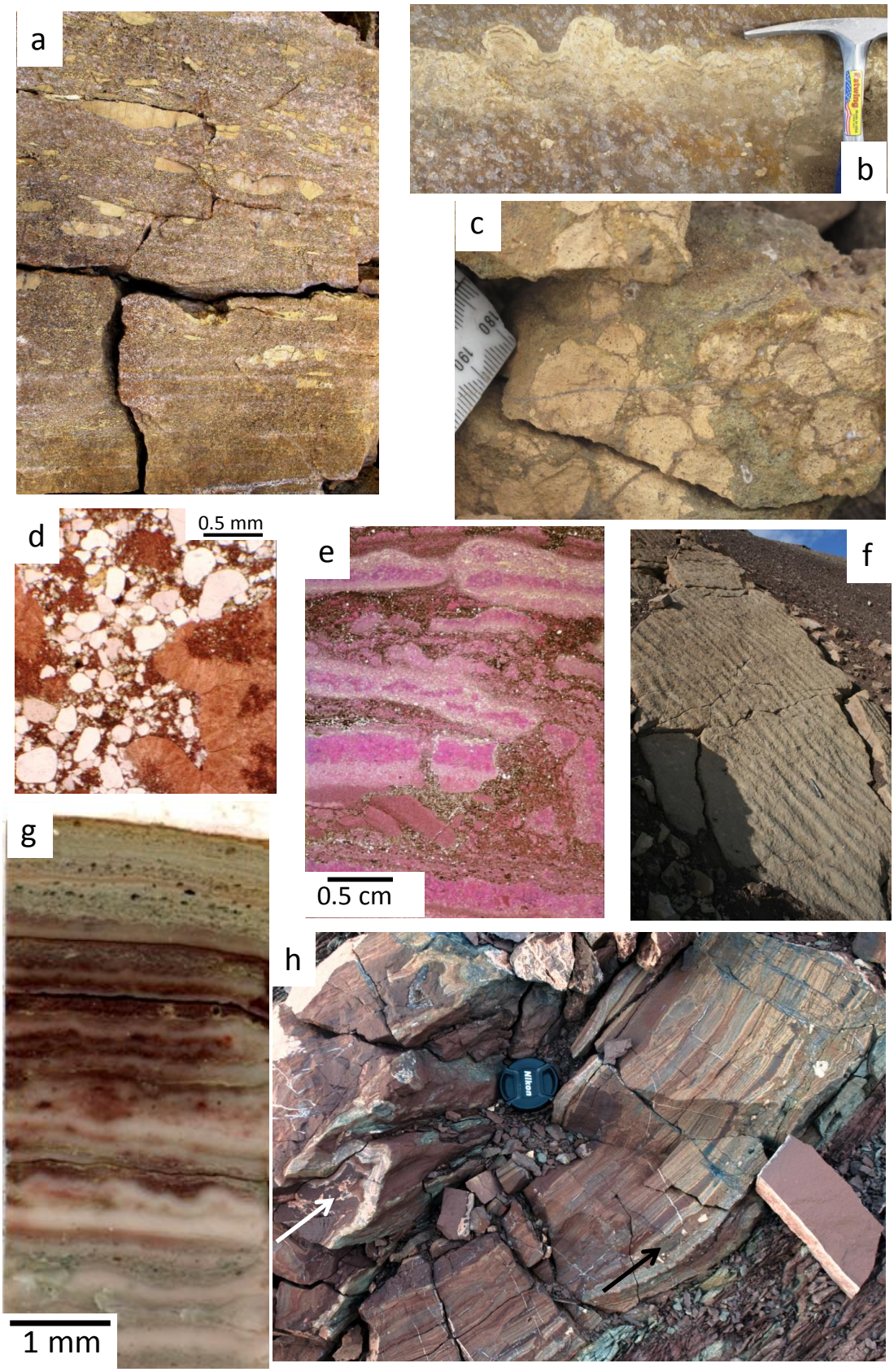

Figure S5. Fluvial and lacustrine facies. Photos (b), (d), (e), (g) and (h) feature limestones carrying a negative $\Delta^{17}O$ anomaly. (a) Cross-stratified medium-grained fluvial channel sandstones, with dolomite clasts derived from periglaciated top of underlying Elbobreen Formation. Base of W1, Ditlovtoppen, width of view 15 cm. (b)

Stromatolitic limestone domes within Fluvial channel facies association, member W2, Dracoisen, hammer for scale. (c) Dolocrete nodules within green fluvial sandstone, Floodplain dolomite facies association, Reinsryggen. The dolocrete has high $\delta^{18}O$ and no $\Delta^{17}O$ anomaly. (d) Fluvial channel facies association. Clasts of limestone with radiaxial fibrous cement reworked within glacifluvial sand, member W2, Dracoisen . Photomicrograph, transmitted light, calcite stained pink with Alizarin Red-S. (e) Carbonate lake margin facies association. Partly brecciated limestone rhythmite with thin sand layers, member W2 Dracoisen, thin section, transmitted light, calcite stained pink with Alizarin Red-S. (f) Carbonate lake margin facies association, sandstone bed with wave ripples (11 cm wavelength), member W2, Dracoisen. (g) Carbonate lake facies association 5. Rhythmic alternations of lacustrine limestone, some laminae developing stromatolitic relief, and ice-rafted glacial debris, member W2, Kvitfjella-Backlundtoppen Ridge, polished unstained hand specimen. (h) Carbonate lake facies association. Limestone laminites with slump folds (white arrow), passing transitionally down to Glacilacustrine Facies Association with individual laminae with ice-rafted pebbles (e.g. black arrow). Member W3, Klofjellet.

2. Additional discussion of geochemical data

Additional details of the geochemical methods can be found in Bao (2006) and Bao and Thiemens (2000). Isotopic data from the carbonate associated sulphate in W2 and W3 are tabulated in Table 1. Trace element data additional to that presented by ref 16 will be presented elsewhere, but as reported earlier, the CAS concentrations are consistently high in the Wilsonbreen carbonates: 1100-4900 ppm sulphate in dolomites and 1400-6400 ppm in calcite.

The CAS data are plotted by facies associations in Figure S6, providing extra information to support the interpretation in the main text. The interpretation follows that of ref 16, but each of the generalizations made in that paper are now supported by a much larger body of data from member W2 as well as new data from W3.

The linear trend in $\Delta^{17}O$-$\delta^{34}S$ space of limestone samples is interpreted as a mixing relationship between pre-existing sulphate, i.e. sulphate dissolved from pre-existing rocks, and new sulphate formed by oxidation of pyrite by non-mass-dependently ^{17}O-depleted O_2. Pre-existing sulphate characteristically lacks a negative $\Delta^{17}O$ value. The light end-member is interpreted as the projection of the mixing line to a $\delta^{34}S$ composition of zero, typical of bulk sulphide minerals during the Sturtian and Marinoan glaciations. Fig. 6 demonstrates that fluvial facies (Facies Association 2) show the most consistently light compositions, but these samples are drawn from a single 3 m-thick bed. There is no other relationship between composition and facies type in the limestones. Dolomite samples lack a distinctly negative $\Delta^{17}O$ value, but in evaporative dolomite facies of Facies Association 3 most samples exhibit extremely positive $\delta^{18}O$ values. These two observations indicate that the sulphate in these samples was affected by microbially mediated sulphate oxygen exchange with water oxygen, erasing the non-mass-dependently depleted ^{17}O signature and imparting corresponding changes to the $\delta^{18}O$ signature.

The data overall display a remarkably consistent pattern, including 7 of the 9 data points from member W3 lying over datapoints from W2. The two outlying data points do not have strongly negative $\Delta^{17}O$ values and so cannot inform on the isotope composition of the light end-member. The most parsimonious explanation for the data is that the light end-member was similar in composition, and hence reflects a similar atmospheric P_{CO_2} in both members W2 and W3.

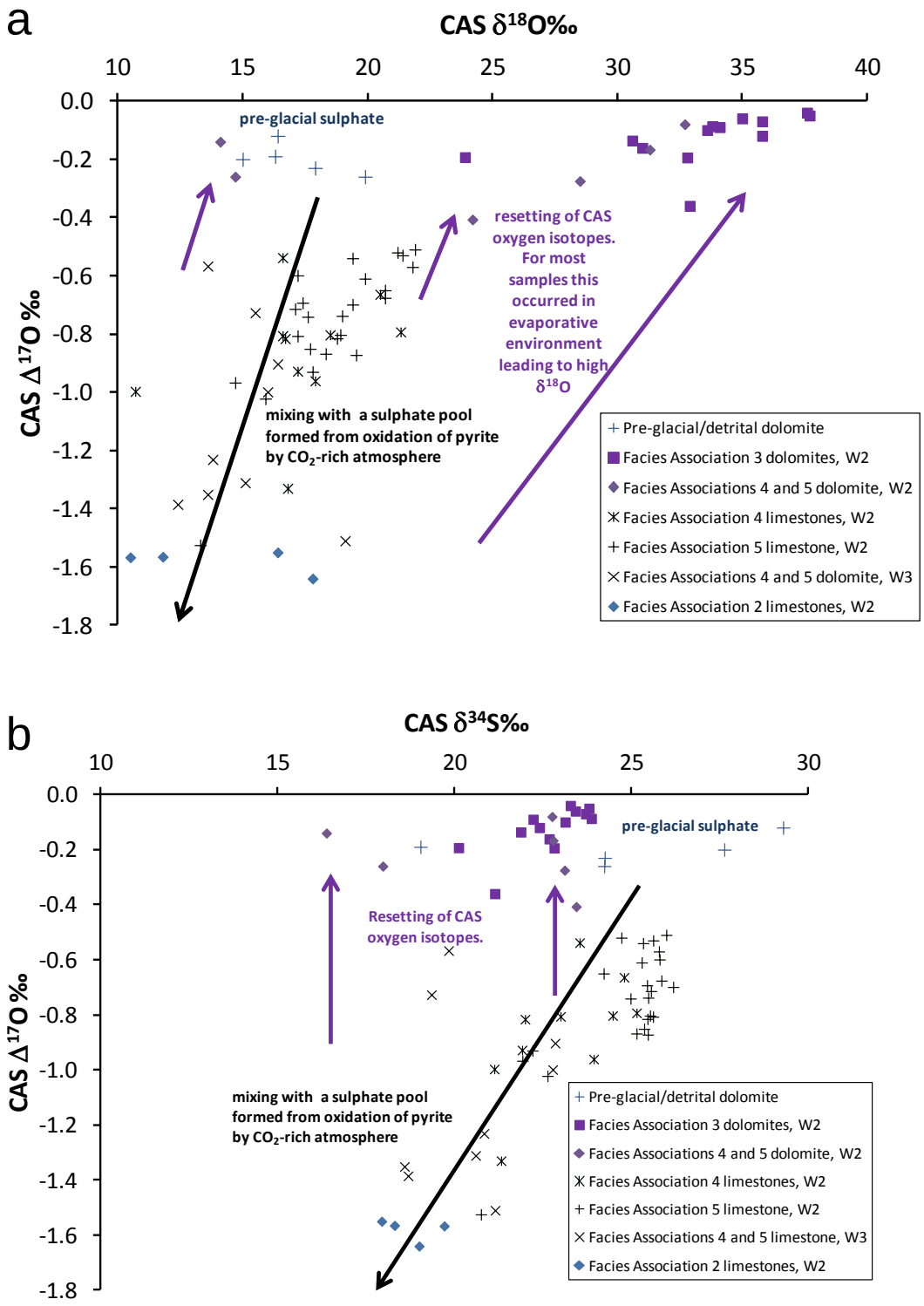

Figure S6. Carbonate-associated sulfate (CAS) data plotted in facies associations with explanation of data trends (also see text). (a) □^{17}O versus □^{18}O. (b) □^{17}O versus 34 □^{34}S. Whereas Figure 2 of the main text only includes pure limestones, this figure includes mixed dolomite-calcite samples that have a more complex history.

Table S1. CAS stable isotope analyses (‰) including those presented in ref. 16. Sulphur isotope compositions from previous work are modified to be consistent with a value of +21.1 ‰ for NBS127. Carbonate mineralogy is shown as D for dolomite, D/C for dolomite-dominated, C for calcite and C/D for calcite dominated. Location codes are shown in Fig. 1 and stratigraphic logs in Fig. S1. Blanks represent insufficient material for analysis. Facies associations are listed in Fig. S3.

Sample number	Member	Height above Formation base, m	Location code	Facies Association	Dominant mineralogy	$\delta^{18}O$	$\Delta^{17}O$	$\delta^{34}S$
F6959	W2	58.50	DRA	2	C	17.8	-1.64	19.00
F6960	W2	58.50	DRA	2	C	16.4	-1.55	17.94
F7117	W2	61.00	DRA	2	C	10.5	-1.57	19.71
F7155	W2	58.30	DRA	2	C	11.8	-1.57	18.30
F6889	W2	115.50	DIT	3	D	33.6	-0.10	23.13
F6891	W2	118.00	DIT	3	D	35.8	-0.07	23.71
F6964	W2	69.60	DRA	3	D/C	32.9	-0.36	21.14
F7144	W2	83.10	DRA	3	D	23.9	-0.19	20.12
F7158	W2	70.00	DRA	3	D	30.6	-0.14	21.88
F7426	W2	118.00	DIT	3	D	33.8	-0.09	23.87
F7648	W2	83.6	REIN	3	D	32.8	-0.19	22.82
F7736	W2	40.00	ORM	3	D	31.0	-0.16	22.68
M4208	W2	82.80	DRA	3	D	37.6	-0.04	23.28
F7127	W2	80.20	DRA	4	D/C			20.49
F7336	W2	61.90	DRA	4	C/D			18.34
F7400	W3 (W2 clast)	123.00	DIT	4	C	10.7	-1.00	21.13
F7430	W2	120.40	DIT	4	D/C	14.7	-0.26	17.97
F7454	W2	120.90	DIT	4	D/C			21.90
F7626	W2	79.09	REIN	4	C/D	20.5	-0.66	24.80
F7628	W2	79.22	REIN	4	C/D	21.3	-0.79	25.15
F7630A	W2	79.40	REIN	4	C	18.5	-0.80	24.47
F7643	W2	82.50	REIN	4	D/C	24.2	-0.41	23.44
F7666	W2	31.00	AND	4	C	17.9	-0.96	23.94
F7687	W2	84.20	KLO-N	4	C/D	16.6	-0.81	23.00
F7688	W2	84.50	KLO-N	4	C/D	16.7	-0.82	22.00
F7689	W2	84.80	KLO-N	4	C	17.2	-0.93	21.91
F7731	W3	85.00	ORM	4	C	15.5	-0.73	19.35
F7732	W3	84.00	ORM	4	C	13.8	-1.23	20.83
F7740	W2	31.40	ORM	4	C	16.6	-0.54	23.54
J1075	W2	31.30	ORM	4	D	32.7	-0.08	22.76
M4210	W2	85.00	DRA	4	C	16.8	-1.33	21.32
EFA126	W3	63.00	AND	5	C	16.4	-0.90	22.85
EFB058	W3	26.00	PIN	5	C/D	13.6	-0.57	19.83
EFK013A	W3	113.00	KLO	5	C	13.6	-1.35	18.59
EFK013B	W3	113.00	KLO	5	C	12.4	-1.39	18.69
F6895	W2	109.00	DIT	5	C	17.8	-0.93	22.21

F7368	W2	80.60	DRA-T	5	C	13.3	-1.53	20.75
F7613	W2	75.30	REIN	5	C/D	15.9	-1.02	22.63
F7632A	W2	79.80	REIN	5	C	18.9	-0.80	25.53
F7632B	W2	79.80	REIN	5	C	19.0	-0.74	25.48
F7636A	W2	80.50	REIN	5	C	18.8	-0.82	25.46
F7636-B	W2	80.50	REIN	5	C	17.2	-0.60	25.80
F7637	W2	80.60	REIN	5	C	17.6	-0.74	24.98
F7638	W2	80.60	REIN	5	C	18.3	-0.87	25.15
F7639	W2	81.00	REIN	5	C	19.5	-0.87	25.47
F7640	W2	81.20	REIN	5	C	16.1		25.54
F7641	W2	81.20	REIN	5	C	17.1	-0.71	25.56
F7642	W2	81.20	REIN	5	C	19.4	-0.70	26.19
F7672	W2	13.50	AND	5	C/D	14.7	-0.97	21.92
F7674	W3	71.00	AND	5	C	19.1	-1.51	21.15
F7675	W3	71.00	AND	5	C	15.1	-1.31	20.60
F7678	W3	63.00	AND	5	C/D	16.0	-1.00	22.78
F7682	W2	67.50	KLO-N	5	C	17.4	-0.69	25.45
F7683	W2	67.20	KLO-N	5	D	28.5	-0.28	23.11
F7685	W2	69.00	KLO-N	5	D	31.3	-0.17	22.79
F7695	W2	73.00	KLO-S	5	C	17.2	-0.81	25.62
F7696	W2	73.50	KLO	5	C	17.7	-0.85	25.37
F7743	W2	31.80	ORM	5	C	20.7	-0.68	25.85
J926	W2	76.90	BAC	5	C	21.8	-0.57	25.78
J928	W2	77.00	BAC	5	C	20.7	-0.65	24.22
J929	W2	77.00	BAC	5	C	19.4	-0.54	25.33
J931	W2	77.15	BAC	5	C	21.2	-0.52	24.72
J948	W2	44.10	GOL	5	D	14.1	-0.14	16.38
J956	W2	38.95	GOL	5	C	21.4	-0.53	25.62
M3765	W2	76.90	BAC	5	C	21.9	-0.51	25.99
M3851	W2	39.40	GOL	5	C	19.9	-0.61	25.30
F6962	W2	69.90	DRA	3D	D	34.1	-0.09	22.23
F6963A-N	W2	69.95	DRA	3S	D	37.7	-0.05	23.81
F6963A-P	W2	69.95	DRA	3S	D	35.8	-0.12	22.40
F6963B	W2	69.95	DRA	3S	D	35.0	-0.06	23.42
J935	W clast	-	GOL	detrital	D	16.3	-0.19	19.04
M3853	W	-	GOL	detrital	D	17.9	-0.23	24.25
M4204	W	-	DRA	detrital	D	19.9	-0.26	24.24

3. Additional model description and coupling procedure

To conduct numerical experiments for Cryogenian conditions, we coupled an atmospheric general circulation model (LMDz; Hourdin et al., 2006) to an ice-sheet model (GRISLI: GRenoble Ice Shelf and Land Ice model; Ritz et al., 2001). The coupling method needs to run LMDz (spatial resolution 4° in latitude x 5° in longitude with 38 vertical levels), with prescribed continental ice, for multiple decades to climatic equilibrium. The ice sheet model (ISM) has a finer grid (40km grid size) and climatic fields of surface air temperature, precipitation and evaporation are downscaled to drive GRISLI. For capturing ice sheet feedbacks with the climate, the general circulation model (GCM) is rerun using the new ice sheet distribution and topography, this procedure being repeated each 10 kyr for investigating orbital forcing (100-200 kyr for computing initial ice sheets).

Lapse-rate corrections are applied to GRISLI to account for the difference between GCM and ISM topography. Although the GCM fully resolves vertical temperature profiles in the atmosphere, to gain computer time we prescribed the lapse rate to be a constant 6 K/km. As can be seen from Figure S7, in contrast with high latitudes, lapse rates in low latitudes remain close to 6K/km throughout the year. This value is reasonable, therefore, for investigating tropical ice sheets. Note that the assumption of a constant lapse rate cannot be applied to mid- or high latitudes. The relative change of precipitation is proportional to the exponential variation of surface temperature.

The ice sheet model GRISLI (Ritz et al., 2001, Peyaud, 2007) is a three-dimensional thermomechanically coupled ISM. With respect to ice flow dynamics, it belongs to the hybrid model type: it includes both the shallow ice approximation (SIA, Hutter, 1983) and the shallow shelf approximation (SSA, MacAyeal, 1989) to solve the Navier-Stokes equations. In this work, we only compute grounded ice, and ice shelves are deactivated.

Surface mass balance (SMB) is the sum of accumulation minus the surface ablation (sublimation plus melting), computed from monthly means of temperature, precipitation and evaporation rate. Melt rate is calculated using the Positive Degree Days (PDD) method, using a standard deviation (σ) of 5°C in order to represent the air temperature excursion over the month (Reeh, 1991). This method has been validated for both Quaternary (Zweck and Huybrechts 2005; Charbit et al. 2007; Pollard et DeConto, 2009) and Neoproteroic ice sheets (ref 20, Donnadieu et al. 2003). PDD methods may slightly under-estimate melt compared with insolation temperature methods (ITM), which also include energy input from solar radiation (Robinson et al., 2010). In the context of the present study, we expect that ITM parameterizations of ablation would increase the sensitivity of tropical ice-sheets to orbital forcing, so the use of the PDD method does not affect our conclusions.

Accumulation rate is defined as precipitation rate minus evaporation rate. LMDz being an atmospheric general circulation model, no sea ice dynamics treatment is specified, the sea ice cover is prescribed and a thickness of 10 meters is imposed. Ice albedo is fixed at 0.6, while snow albedo varies from 0.9 from 0.55 as a function of the zenith, and ageing process (Marshall and Oglesby 1994). Land ice/snow free surface has the characteristic of a bare soil (rocky regolith) with an albedo of 0.3.

Boundary conditions and simulations performed to build up initial ice-sheets
Numerical experiments include a solar constant set to 0.94 of the present (Gough, 1981) and paleogeography reconstruction in which the East Svalbard region occupies a tropical location ~ 20°S (Fig. S8) (32). Given the uncertainty in the topography, we prescribe a maximum elevation of 2000 m for mountain chains, while the elevation of the lowlands is fixed at 200 m. To be consistent with the classical snowball Earth theory (i.e hard/full snowball Earth), we assume that oceans are entirely ice-covered.

For reconstructing the pre-existing ice sheet, formed during the early stage of the Cryogenian ice age, LMDz is run starting from ice free conditions over continents and low content of atmospheric CO_2 (0.1 mbar). Orbital parameters are set at their present day values (eccentricity: 0.016, obliquity: 23.4, degrees between spring equinox/perihelion = 102.7°) and the Earth's rotation rate is left unchanged (24 hours). Since the weakness of hydrological cycle (Pierrehumbert et al. 2011) slows the growth of the initial ice-sheet, a more economical parameterization is used for gaining time. For artificially increasing the accumulation rate, we neglect the evaporation from 0 to 500kyrs. The pre-existing ice sheet volume calculated by this procedure is shown in Fig. S9. After 500kyrs, the initial parameterization is reestablished and used for computing an ice sheet at the equilibrium with snowball earth's climate.

Starting from 500kyrs and using 0.1 mbar of pCO_2, more than 600 kyrs are required to converge on a final equilibrium for climate and ice sheet size. At the steady state the ISM generates an ice volume close to 1.7×10^8 km^3 (~3 times the LGM ice-sheet volume, Fig. S9 and Fig. S10), and these values are in agreement with previous works (ref. 20; Donnadieu et al. 2003). The initial ice sheet surrounds low latitudes areas, except for isolated equatorial coastal regions (Fig. S10a). The presence of elevated terrain allows ice to penetrate the equatorial band despite a negative annual precipitation and evaporation-sublimation budget.

Orbital forcing experiments
Because the sedimentological evidence illustrate repeated glacial advance and retreat in low latitudes, we focused on potential processes able to affect ice dynamics of tropical ice sheets. Initial sensitivity experiments were performed using eccentricity, precession and obliquity cycles characteristic of the Quaternary and pCO_2 = 100 mbar (Table S2). These confirmed that obliquity produces a negligible effect in low latitudes, in contrast with precession (Fig. S11; cf. ref. 26). Consequently, in the present study we focused on the influence of precessional cycles on tropical ice sheets.

	PD	run 1	run 2	run 3	run 4	run 5	run 6
Eccentricity	0.016715	0.00	0.06	0.06	0.06	0.06	0.00
Precession	102.7	90.0	90.0	270.0	270.0	90.0	90.0
Obliquity	23.441	22.5	22.5	22.5	24.5	24.5	24.5

Table S2: Eccentricity, precession and obliquity values used in the sensitivity experiments. PD denotes present-day values.

In the orbital forcing experiments, we switched between two extremes of the precession cycle favoring cold and warm summers, respectively, over the northern tropics (CSO: cold summer orbit and WSO: warm summer orbit; Fig. S14). We used a cycle length of 10,000 years, although for the purposes of demonstrating that precession can drive ice-

sheet fluctuations, the cycle length is not crucial so long as it exceeds ice-sheet response time. Recent work, however, indicates that orbital cycles in the Precambrian were not dissimilar in length to modern Milankovitch cycles (Zhang et al., 2015).

As in the case of the initialization runs, we used a coupling interval of 10 kyr between the GCM and ISM. A shorter coupling interval may be desirable, but would greatly increase the computational expense of runs performed by the ice-sheet model (ISM). However, we believe that the coupling interval of 10 kyr is justifiable due to the weakness of the hydrological cycle during a Snowball event (Pierrehumbert et al. 2011). This limits the efficiency of processes governing ice sheet extent and volume, such that several kyr are required for changes in orography and ice extent to have significant influence on climate. A sensitivity test performed with a longer coupling interval (20 kyr instead of 10 kyr; Fig. S12) reveals that, for the same orbital forcing, the ice sheet response is amplified (volume) but ice extent remains unchanged.

For initialization experiments, the problem is quite different. The duration of the coupling interval is less important because initialization runs are conducted to obtain an ice sheet in equilibrium with the climate. In this case, the coupling interval can exceed 100 kyr. The time required for equilibrating the ice sheet under LMDz climate can be seen in Fig. S9).

The GCM was run between coupling intervals until a steady state was reached (typically tens of years). Climatic variables were averaged over 5 years following establishment of the steady state. Time steps were 30 minutes for the GCM. For GRISLI, we applied an adjustable "short" time step of about 1 day for the mass-conservation equation because of its potential instability. Solutions for the heat equation, bedrock reaction and surface mass balance were computed with a longer time step (5 years).

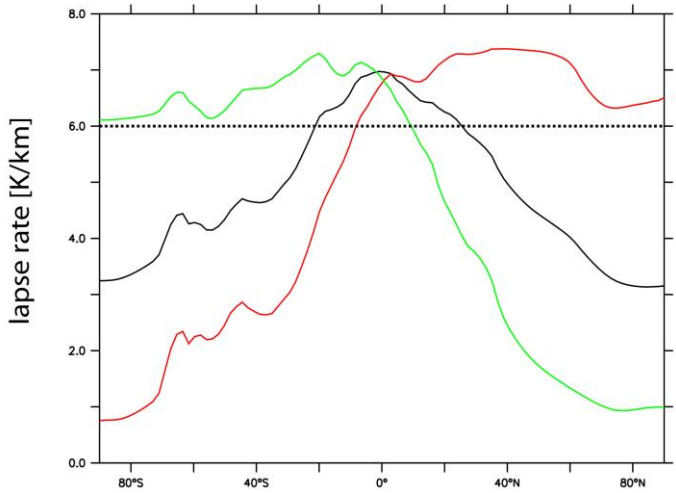

Figure S7. Lapse rates calculated by LMDz using CSO configuration between the surface and 5.5 km (above the maximum ice sheet elevation) for 20 mbar of pCO_2. The black curve represents the annual mean value, red/green lines are the calculation for summer in northern/southern hemisphere respectively. The dashed line represents the lapse rate used by GRISLI.

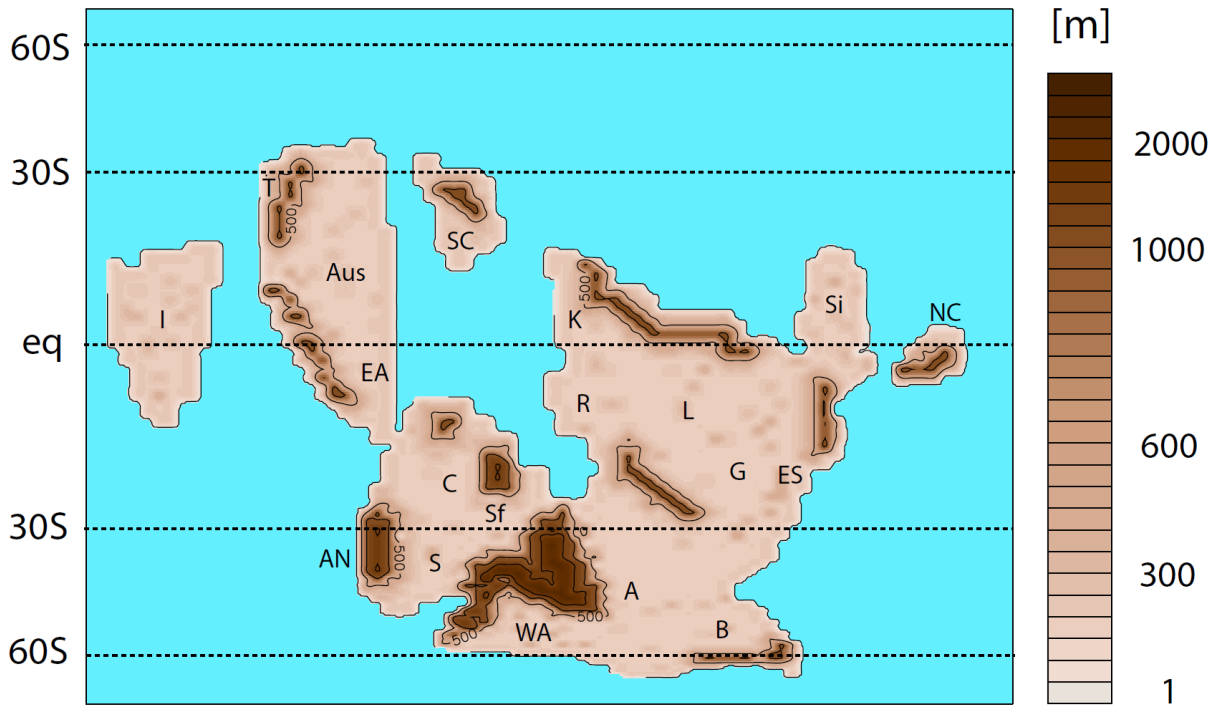

Craton/terrane name abbreviations: A—Amazonia; AN—Arabia—Nubia; B—Baltica; C—Congo; EA—East Antarctica; ES—East Svalbard; G—Greenland; I—India; K—Kalahari; L—Laurentia; NC—North China; R—Rio Plata; S—Sahara; Aus—Australia; SC—South China; Sf—Sao Francisco; Si—Siberia; T—Tarim; WA—West Africa.

Figure S8. Continental configurations used in the modelling experiments. After ref. (22).

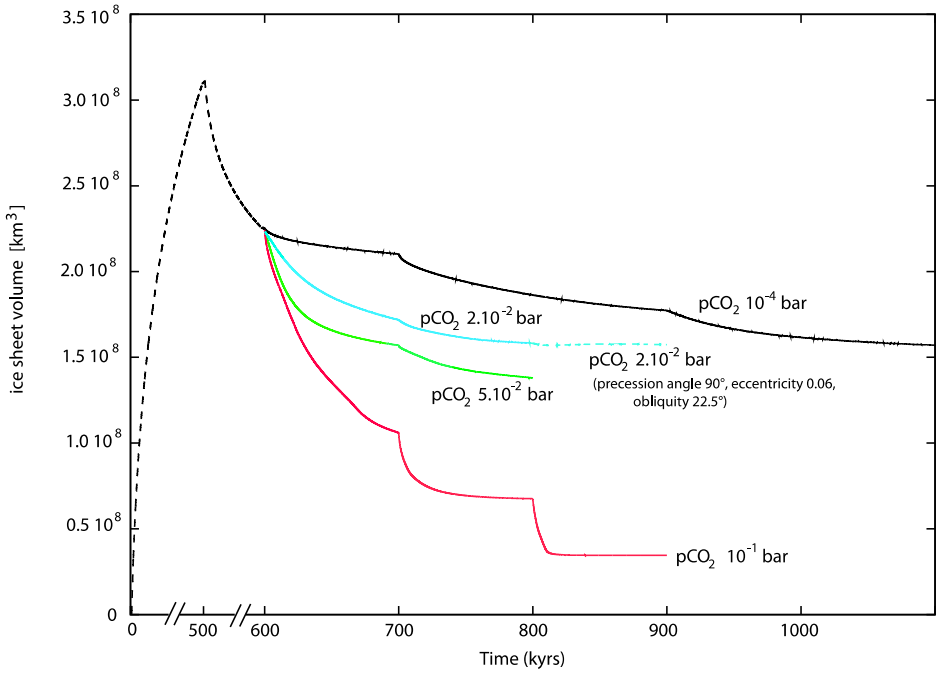

Figure S9. 3D ice sheet model results showing total ice volume versus time through a range of pCO_2 values (10^{-4}, 2.10^{-2}, 5.10^{-2} and 10^{-1} bar) using present day orbital parameters: eccentricity 0.016 precession 102°: obliquity 23.5° (excepted blue dash line).

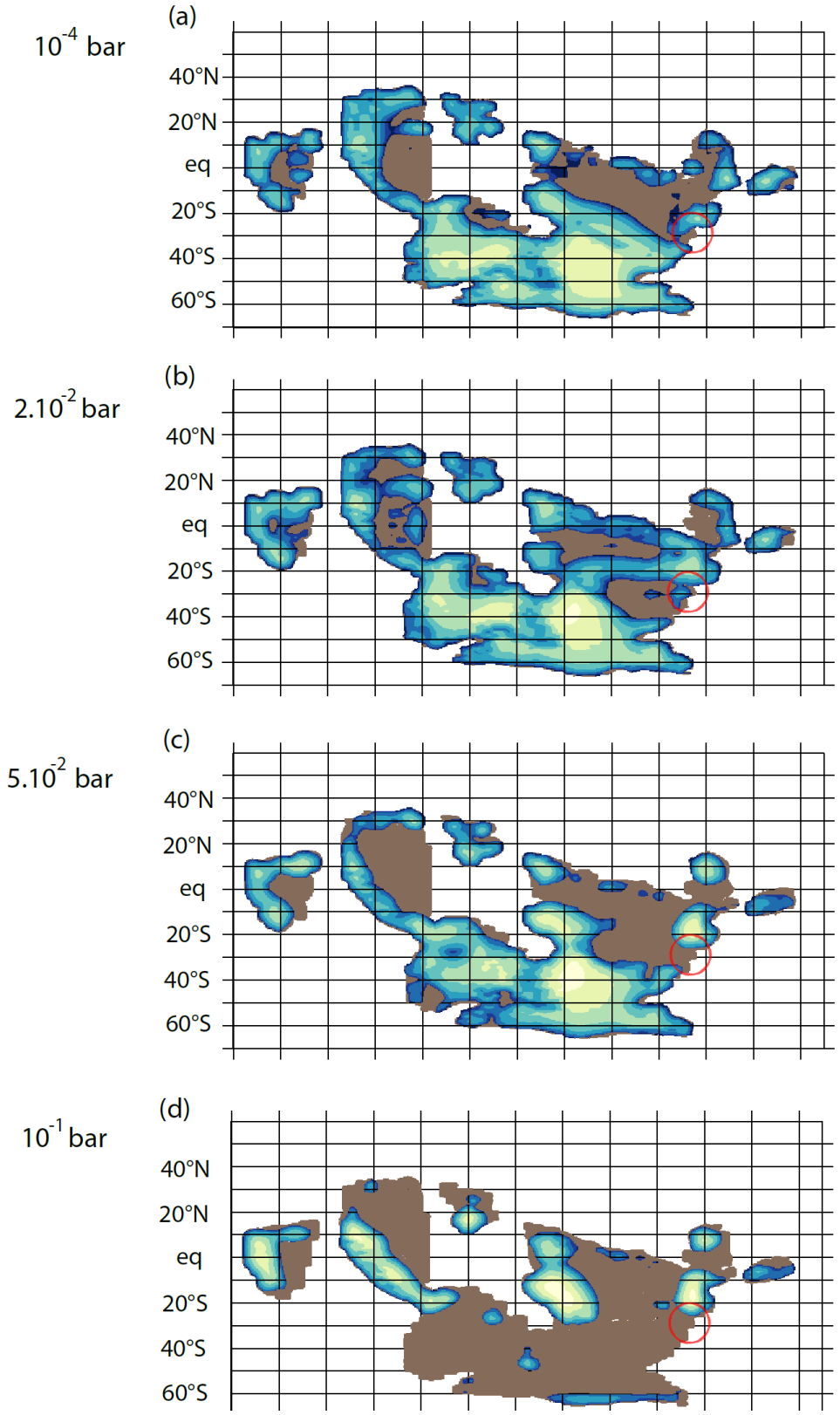

Figure S10. Ice thickness (m) for ice sheet/climate equilibrium obtained with different pCO_2 values: (a) (a) 0.1, (b) 20, (c) 50 and (d) 100 mbar. Orbital parameters as in Fig. S9. Brown color represents ice-free land surface. Svalbard location is indicated by red circle.

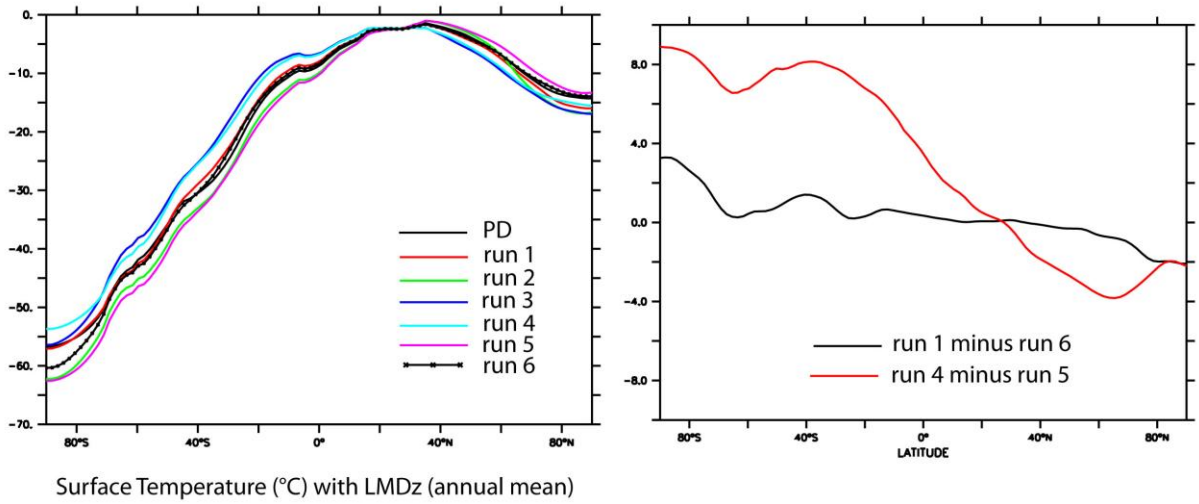

Figure S11: A set of sensitivity experiments performed with LMDz showing the respective role of each astronomical parameter. Run 1 minus run 6 shows the effect of changing obliquity from 22° to 24.5° while holding other parameters constant, while run 4 minus run 5 isolates the effect of the precession cycle.

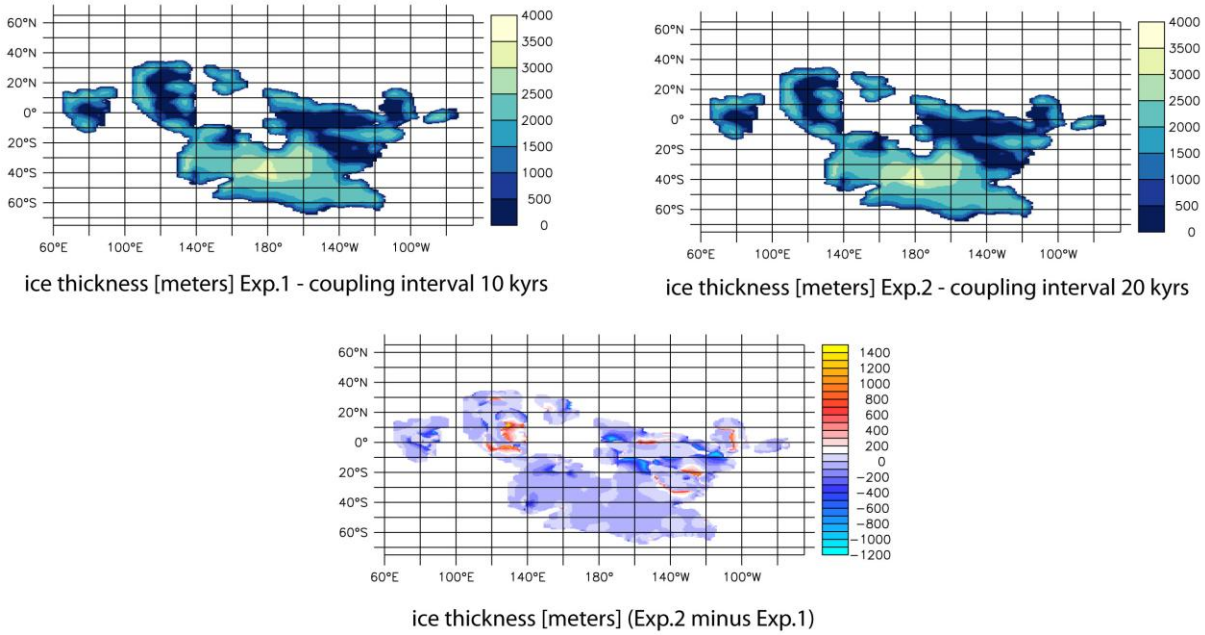

Figure S12: Ice thickness predicted for 20 mbar of pCO_2 for two different coupling intervals. Exp. 1 and Exp. 2 are performed using the same orbital forcing: WSO for 10 or 20 kyr then CSO during 10 or 20 kyr respectively.

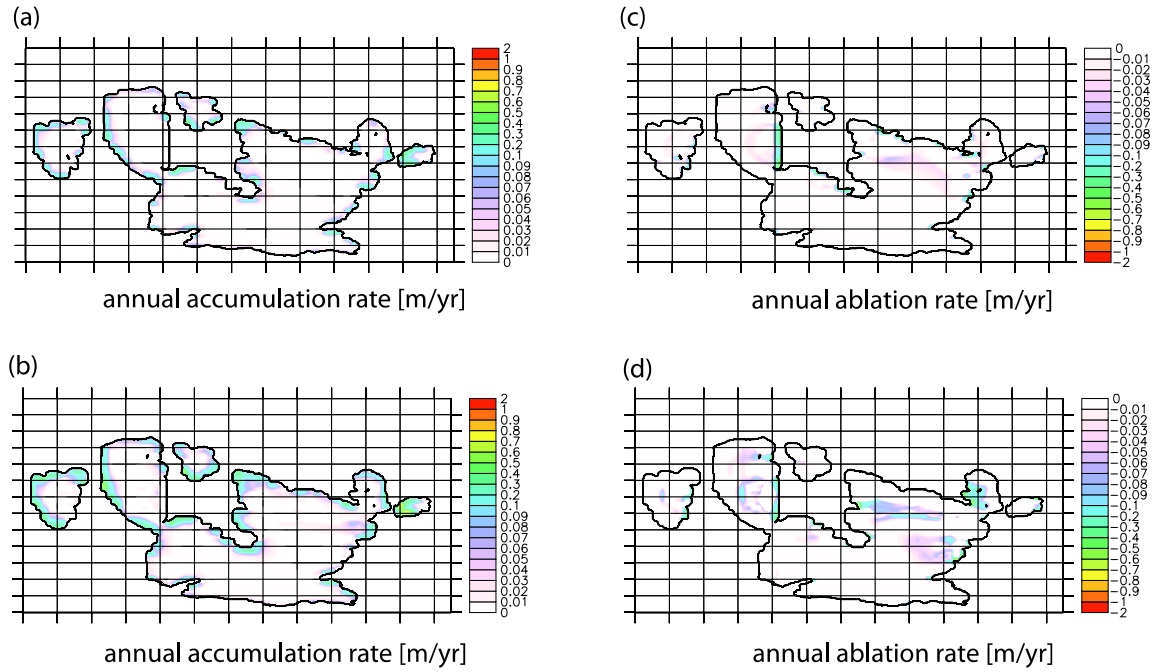

Figure S13. Annual accumulation and ablation rates for pCO_2 = 0.1 mbar (a and c); and 20 mbar (b and d). Orbital parameters as in Fig. S9.

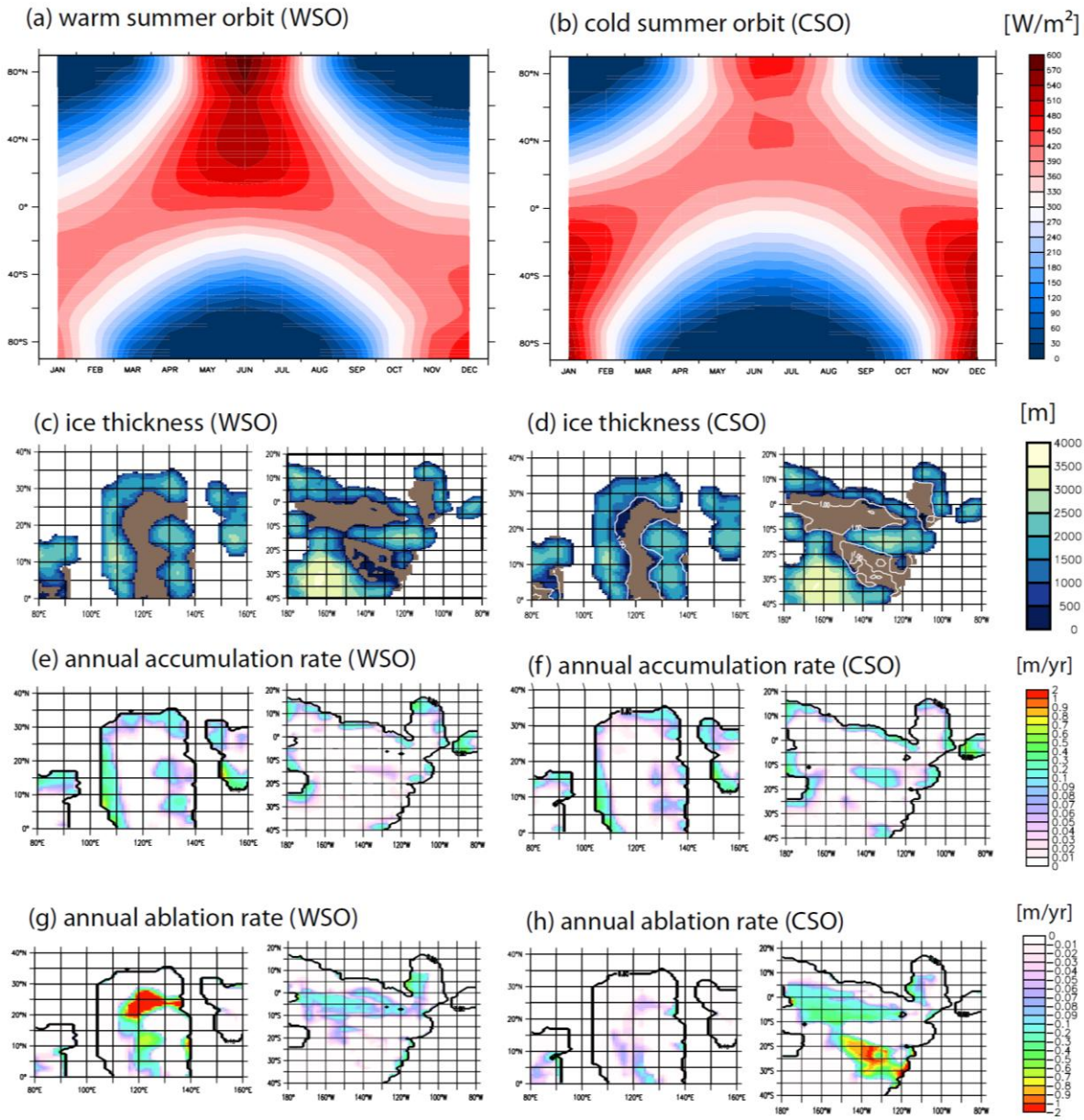

Figure S14. (a) Incoming solar radiation at top of atmosphere (W/m^2) for a warm summer orbit for the northern hemisphere (WSO), fixing the perihelion in June (precession angle 270°) and (b) for a cold summer orbit (CSO), fixing the perihelion in December (precession angle 90°). Eccentricity and obliquity are held constant to 0.06 and 22.5° respectively. (c) Ice thickness for 20 mbar of carbon dioxide for a WSO (after 20 kyrs of simulation) and (d) for a CSO (after 30 kyrs of simulation). Light brown color denotes ice-free continental areas, the white line represents the old ice sheet extent (WSO case). (e) (f) (g) (h) accumulation/ablation rates (annual mean) computed by the ice-sheet model for WSO (after 20 kyrs of simulation) and CSO (after 30 kyrs of simulation).

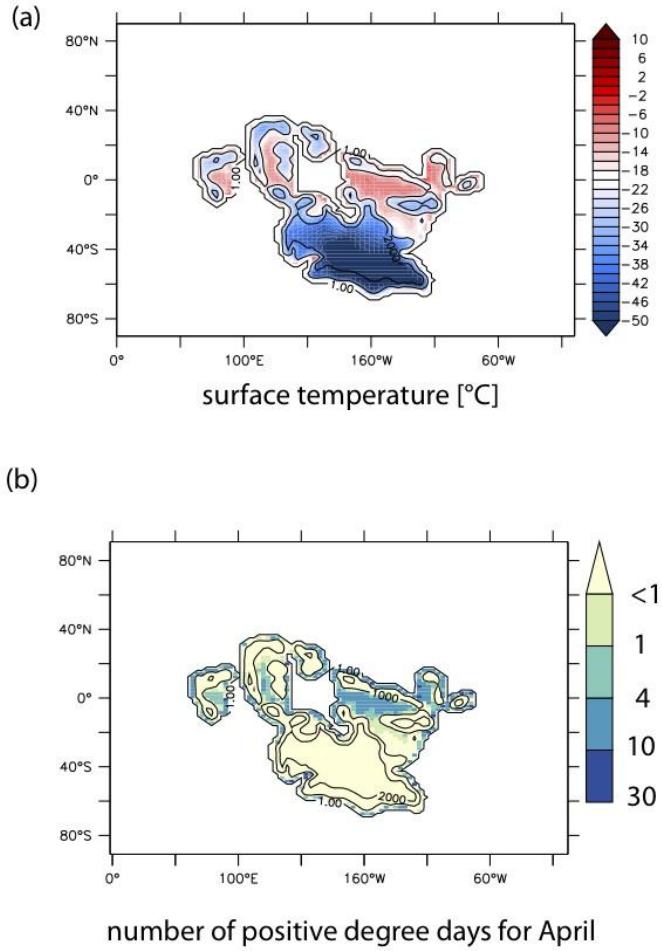

Figure S15: (a) monthly continental surface temperature for April [daily output] using 20 mbar of pCO_2 and a WSO orbital configuration. Black lines show elevation [1, 1000 and 2000 meters]. (b) Number of positive degree days for April using a standard deviation (σ = 5°C) for air temperature excursion.

Movie S1 (separate file): ice-sheet advance/retreat linked to Milankovitch orbital cycles during a snowball event.
Description : changes in land ice extent obtained with 20 mbar of carbon dioxide in response to changes of orbital forcing (WSO and CSO, warm/cold summer orbit for the northern hemisphere) over the course of two precession cycles (40 kyrs of simulation).

References not in the main text

Bao, H.M. 2006 Purifying barite for oxygen measurement by dissolution and reprecipitation in a chelating solution. *Anal. Chem.*, 78, 304-309.

Bao, H.M., Thiemens, M.H. 2000 Generation of O_2 from $BaSO_4$ using a CO_2-laser fluorination system for simultaneous analysis of delta O-18 and delta O-17. *Anal. Chem.* , 72, 4029-4032.

Benn, D.I. and Ballantyne, C.K. 1993. The description and representation of particle shape. *Earth Surface Processes and Landforms* 18, 665-672.

Benn, D.I. 1994. Fabric shape and the interpretation of sedimentary fabric data. *Journal of Sedimentary Research* A64, 910-915.

Benn, D.I. and Evans, D.J.A. 2010. Glaciers and Glaciation, 2nd edition. Hodder Education, London, 802 pp.

Charbit, S., Paillard D. and Ramstein, G. 2008. Amount of CO_2 emissions irreversibly leading to the total melting of Greenland. Geophysical Research Letters 35, DOI: 10.1029/2008GL033472.

Donnadieu,Y., Fluteau, F., Ramstein, G., Ritz, C. and Besse, J. 2003. Is there a conflict between the Neoproterozoic glacial deposits and the Snowball Earth interpretation: an improved understanding with numerical modeling. Earth and Planetary Science Letters 208, 101-112.

Domack, E. W. and Lawson, D. E. 1985. Pebble fabric in an ice rafted diamicton. Journal of Geology 93, 577–92.

Gough, D.O., 1981, Solar interior structure and luminosity variations: Solar Physics, v. 74, p. 21-34.

Hourdin, F., Musat, I., Bony, S., Braconnot, P., Codron, F., Dufresne, J.-L., Fairhead, L., Filiberti, M.-A., Friedlingstein, P., Granspeix, J.-Y., Krinner, G., Van, P.L., Li, Z.-X. and Lott, F. 2006. The LMDZ4 general circulation model: climate performance and sensitivity to parameterized physics with emphasis on tropical convection. Climate Dynamics 27, 787-813.

Hutter, K.: 1983. Theoretical Glaciology: Material Science of Ice and the Mechanics of Glaciers and Ice Sheets, Springer, 548 pp.,

Knight, J. 2008. The environmental significance of ventifacts: a critical review. Earth-Science Reviews 86, 89-105.

MacAyeal. 1989 D.R.. Large-scale ice flow over a viscous basal sediment: Theory and application to Ice Stream B, Antarctica. Journal of Geophysical Research, 94(B4):4071--4087.

Marshall, S., and Oglesby, R.J., 1994, An improved snow hydrology for Gcms.1. Snow cover fraction, albedo, grain-Size, and age: Climate Dynamics, v. 10, p. 21-37.

Peyaud, V., Ritz, C., and Krinner, G. 2007. Modelling the Early Weichselian Eurasian Ice Sheets: role of ice shelves and influence of ice-dammed lakes, Clim. Past, 3, 375–386, doi:10.5194/cp-3-375-2007.

Pierrehumbert, R.T., Abbot D.S., Voigt, A. and Koll, D., 2011. Climate of the Neoproterozoic . Annual Review of Earth and Planetary Sciences 39: 417-460, DOI:10.1146/annurev-earth-040809152447.

Pollard, D and DeConto, R.M. 2009. Modelling West Antarctic ice sheet growth and collapse through the past five million years. *Nature* **458**, 329-332 (2009).

Powell, R.D. and Alley, R.B. 1997. Grounding-line systems: processes, glaciological inferences and the stratigraphic record. Antarctic Research Series, Vol. 71, 169-187

Reeh, N. 1991. Parameterization of melt rate and surface temperature on the Greenland ice sheet. Polarforschung,59(3), 113–128.

Ritz, C., Rommelaere, V. and Dumas, C. 2001. Modeling the evolution of Antarctic ice sheet over the last 420,000 years: implications for altitude changes in the Vostok region. Journal of Geophysical Research doi: 10.1029/2001JD900232.

Robinson, A., Calov, R. and Ganopolski, A. 2010. An efficient regional energy-moisture balance model for simulation of the Greenland Ice Sheet response to climate change. The Cryosphere, 4, 129–144.

Zhang, S., Wang, X., Hammarlund, E.U., Wang, H., Costa, M.M., Bjerrum, C.J., Connelly, J.N., Zhang, B., Bian, L. and Canfield, D.E. 2015. Orbital forcing of climate 1.4 billion years ago. PNAS 112, doi: 10.1073/pnas.1502239112.

Zweck, C. and Huybrechts, P. 2005. Modeling of the northern hemisphere ice sheets during the last glacial cycle and glaciological sensitivity. Journal of Geophysical Research Atmospheres 110, DOI: 10.1029/2004JD005489.